JOURNAL OF THE AMERICAN CHEMICAL SOCIETY

Article

pubs.acs.org/JACS

Self-Assembly of Amphiphilic Plasmonic Micelle-Like Nanoparticles in Selective Solvents

Jie He,[†,#] Xinglu Huang,[‡,#] Yan-Chun Li,[∥] Yijing Liu,[†] Taarika Babu,[†] Maria A. Aronova,[§] Shouju Wang,[‡] Zhongyuan Lu,*[,∥] Xiaoyuan Chen,*[,‡] and Zhihong Nie*[,†]

[†]Department of Chemistry and Biochemistry, University of Maryland, College Park, Maryland 20742, United States

[‡]Laboratory of Molecular Imaging and Nanomedicine (LOMIN) and [§]Laboratory of Cellular Imaging and Macromolecular Biophysics, National Institute of Biomedical Imaging and Bioengineering (NIBIB), National Institutes of Health (NIH), Bethesda, Maryland 20892, United States

[∥]State Key Laboratory of Theoretical and Computational Chemistry, Institute of Theoretical Chemistry, Jilin University, Changchun, 130023, China

Supporting Information

ABSTRACT: Amphiphilic plasmonic micelle-like nanoparticles (APMNs) composed of gold nanoparticles (AuNPs) and amphiphilic block copolymers (BCPs) structurally resemble polymer micelles with well-defined architectures and chemistry. The APMNs can be potentially considered as a prototype for modeling a higher-level self-assembly of micelles. The understanding of such secondary self-assembly is of particular importance for the bottom-up design of new hierarchical nanostructures. This article describes the self-assembly, modeling, and applications of APMN assemblies in selective solvents. In a mixture of water/tetrahydrofuran, APMNs assembled into various superstructures, including unimolecular micelles, clusters with controlled number of APMNs, and vesicles, depending on the lengths of polymer tethers and the sizes of AuNP cores. The delicate interplay of entropy and enthalpy contributions to the overall free energy associated with the assembly process, which is strongly dependent on the spherical architecture of APMNs, yields an assembly diagram that is different from the assembly of linear BCPs. Our experimental and computational studies suggested that the morphologies of assemblies were largely determined by the deformability of the effective nanoparticles (that is, nanoparticles together with tethered chains as a whole). The assemblies of APMNs resulted in strong absorption in near-infrared range due to the remarkable plasmonic coupling of Au cores, thus facilitating their biomedical applications in bioimaging and photothermal therapy of cancer.

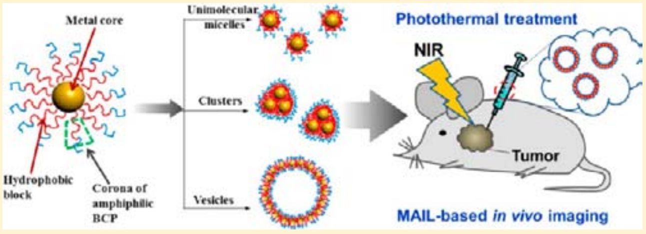

1. INTRODUCTION

Micellar architectures assembled from block copolymers (BCPs) have emerged as a remarkable class of building blocks for a higher-level (secondary) self-assembly of complex hierarchically structured materials.[1−7] For instance, Janus-like amphiphilic micelles were used as building blocks to assemble into nanoscale tubular and sheet-like superstructures.[7] Monodispersed multicompartment polymer micelles assembled from ABC triblock terpolymers can further organize into segmented cylindrical nanostructures.[1] Amphiphilic cylindrical ABC triblock comicelles can self-assemble into hierarchical supermicelle architectures at a larger length scale.[2] However, to date, our ability to assemble micellar architectures into complex superstructures is still very limited, compared to the "first-level" self-assembly of BCPs.[8,9] This is largely due to: (i) the challenges in preparing well-defined building blocks with controlled homogeneity which is critical for the higher level assembly, (ii) the limited understanding of secondary assembly regarding thermodynamics, kinetics, and mechanism of assembly, and (iii) the difficulty in characterizing the spatial organization of individual building blocks in assemblies, especially for pure polymer systems.[10−12]

Despite tremendous efforts to further enhance the complexity of micelles, a simple yet effective model is urgently needed for exploring the design rules that govern the aggregation of micelles into desired superstructures. Ideally, such building blocks should illustrate the well-defined chemistry and architectures of BCP micelles. Recently, inorganic nanoparticles (NPs) tethered with polymers have emerged as a new class of building blocks for the fabrication of various superstructures with interesting optoelectronic properties.[13−25] In particular, building blocks containing a rigid metal core tethered with multiple amphiphilic BCPs are structurally equivalent to BCP micellar architectures composed of a bulky core and a corona of multiple flexible amphiphilic BCP chains.[15,26,27] Their architecture is significantly different from that of single polymer chain or a mixture of polymers modified NPs.[14,16] Such

Received: February 25, 2013
Published: May 5, 2013

dx.doi.org/10.1021/ja402015s | *J. Am. Chem. Soc.* 2013, 135, 7974−7984

building blocks, which have well-defined structure and surface chemistry (e.g., the lengths, chemical compositions, and grafting density of polymer tethers), allow us to simplify and model the structural complexity of polymer micelles. The understanding of their assembly behaviors may provide new insights into the secondary self-assembly of polymer micellar architectures in selective solvents. The use of NPs as scaffolds to bring multiple BCPs together in a controlled manner offers a straightforward yet powerful way to create micelle-like architectures with well-defined chemistry but without multistep synthesis and self-assembly. In addition, the presence of gold NPs (AuNPs) as the "micelle" cores endows the localized surface plasmon resonance (LSPR) properties to such building blocks (referred as, amphiphilic plasmonic micelle-like nanoparticles (APMNs)). The controlled assembly of such APMNs enables one to modulate the plasmon coupling between individual building blocks,[28] thus the collective properties of assemblies.[21,29−31]

Herein, we report the self-assembly and modeling of APMNs composed of AuNPs and linear amphiphilic BCPs in selective solvents. The ability to assemble APMNs in selective solvents enables one to fully explore the critical role of kinetic and thermodynamic factors in the assembly process, which cannot be achieved using assembly by film hydration method reported previously.[15,16] The APMNs assembled into various superstructures including unimolecular micelles, clusters with controlled number of APMNs, and vesicles composed of a single layer of APMNs in the membrane in a mixture of water/tetrahydrofuran (THF). The assembly of APMNs with spherical architectures (that is, BCP chains spherically distributed on a rigid NP core) illustrates a new assembly diagram that is different from the conventional assembly of linear BCPs. With the increase in the length of polymer tethers or the decrease in the size of NP cores, the self-assembly of APMNs underwent morphological transition from unimolecular micelles, to clusters, and to vesicles. Such morphological transition cannot be interpreted by using the conventional packing theory which is widely used for molecular amphiphiles. Our computational studies suggest that the assembly morphologies are largely determined by the deformability of the effective NPs (that is, NP together with tethered chains as a whole), which has been rarely explored previously.[32] The controllable plasmonic coupling of AuNPs in the assemblies resulted in a drastic red-shift of the LSPR peak and a significant enhancement of LSPR absorption in the near-infrared (NIR) range. We further demonstrated that such assembled nanostructures are attractive candidates for in *vitro* and *vivo* cancer imaging and photothermal therapy.

2. EXPERIMENTS

2.1. Materials. Azobis(isobutyronitrile) (AIBN), styrene, 4-cyano-4-(phenylcarbonothioylthio)pentanoic acid (CPPA), gold(III) chloride trihydrate ($HAuCl_4$, ≥99.9% trace metals basis), sodium borohydride ($NaBH_4$, ≥99%), and sodium citrate tribasic dihydrate (≥99%) were purchased from Sigma-Aldrich. All the chemicals were used as received unless otherwise noted. Poly(ethylene oxide) methyl ether (PEG) (molecular weight, M_w, 2000 g/mol, Sigma-Aldrich) was purified by precipitation in ethyl ether before use. AIBN was recrystallized from ethanol. Styrene was distilled under vacuum prior to use and stored in freezer at −20 °C. Deionized water (Millipore Milli-Q grade) with resistivity of 18.0 MΩ was used in all the experiments.

2.2. Synthesis of BCPs and AuNPs. Amphiphilic BCPs of poly(ethyl oxide)-*b*-polystyrene with a thiol group at polystyrene end (PEO-*b*-PS-SH) were synthesized following the RAFT polymerization procedures reported previously.[15] The PEO-*b*-PS-SH samples were designed with different polystyrene (PS) lengths and a fixed PEG M_w of 2000 g/mol. The lengths of PS blocks were 7.7, 13.9, 23.9, 25.7, 33.6, and 49.3 k, as measured by gel permeation chromatography (GPC) and proton nuclear magnetic resonance (^{1}H NMR). The reduction of dithioester to thiol end groups in BCPs in the presence of *n*-butyl amine was confirmed by UV−vis spectra.

AuNPs were synthesized using methods reported previously. AuNPs with 5 nm diameter were obtained using the one-step direct synthesis.[33] AuNPs with diameters of 14, 20, 30, and 40 nm were prepared by sodium citrate reduction method.[34] Using 14 nm AuNPs as an example, a 100 mg of $HAuCl_4$ was dissolved in 1 L of H_2O and heated to boiling under stirring. A 30 mL of sodium citrate (1 wt %) solution was then quickly injected. The reaction mixture was refluxed for 30 min. The AuNPs were then collected by centrifugation. The 14 nm AuNPs were used as seeds to further grow larger AuNPs in the presence of sodium citrate at 80 °C. By varying the concentration of $HAuCl_4$, AuNPs with different diameters of 20, 30, and 40 nm were prepared accordingly.

2.3. Surface Modification and Self-Assembly of AuNPs. The surface modification of 5 nm AuNPs was performed using interfacial ligand-exchange method. Typically, 5 mg of PEO-*b*-PS-SH was first dissolved in 10 mL of toluene or chloroform which is immiscible with water. After adding this solution to an aqueous solution of 5 nm AuNPs, the mixture was sonicated for 2 h under room temperature. The formed emulsion was kept undisturbed overnight until the water phase became colorless. The oil phase containing AuNPs was then collected and dried under vacuum at 40 °C. The BCP modified AuNPs were dispersed in THF and further purified by centrifugation in THF/water/ethanol (2:1:2, vol %) for 6 cycles. The surface modification of AuNPs with diameters of 14, 20, 30, and 40 nm was performed in the DMF/THF mixed solvents.[15] A 5 mg of thiol-ended PEO-*b*-PS was dissolved in 10 mL of DMF/THF (1:1, vol %). A concentrated solution of AuNPs (∼2 mg/mL) was added dropwise into the above solution under vigorous shaking. The mixture was then sonicated for 30 min and kept for 6 h to allow ligand exchange. AuNPs were further purified by centrifugation for 6−8 times and redispersed in THF at 1 mg/mL. The concentration was calculated from the absorption of AuNPs based on the theoretical extinction coefficient.[35]

The self-assembly of APMNs was triggered by slowly adding water into a THF solution of APMNs (∼0.5 mg/mL unless otherwise stated) until the water content reached a targeted concentration. The mixed solution was gently stirred (100 rpm) for 2 h and then dialyzed (dialysis bags with the M_w cutoff of 3000−5000 g/mol) against water to remove the organic solvents for 24 h. The self-assembled nanostructures were then examined by electron microscopes.

2.4. Model and Simulation Method. *Mesoscale Simulation Method: Dissipative Particle Dynamics (DPD).* DPD simulation technique was proven to be a suitable and efficient method in the studies of self-assembly of BCPs[36,37] and NPs.[38,39] In DPD method (see SI for more detailed description), the time evolution of the interacting coarse-grained (CG) beads is governed by Newton's equations of motion:[40]

$$\frac{\mathrm{d}\vec{r}_i}{\mathrm{d}t} = \vec{v}_i$$

$$\frac{\mathrm{d}\vec{v}_i}{\mathrm{d}t} = \sum_{j\neq i} (\vec{F}_{ij}^{\mathrm{C}} + \vec{F}_{ij}^{\mathrm{D}} + \vec{F}_{ij}^{\mathrm{R}}) = \vec{f}_i \tag{1}$$

Interbead interactions are characterized by pairwise conservative, dissipative, and random forces. They are

$$\vec{F}_{ij}^{\mathrm{C}} = \alpha_{ij}(1 - r_{ij}/r_{\mathrm{c}})\vec{e}_{ij}$$

$$\vec{F}_{ij}^{\mathrm{D}} = -\gamma w^{\mathrm{D}}(r_{ij})(\vec{e}_{ij}\cdot\vec{v}_{ij})\vec{e}_{ij}$$

$$\vec{F}_{ij}^{\mathrm{R}} = \sigma w^{\mathrm{R}}(r_{ij})\theta_{ij}\vec{e}_{ij} \tag{2}$$

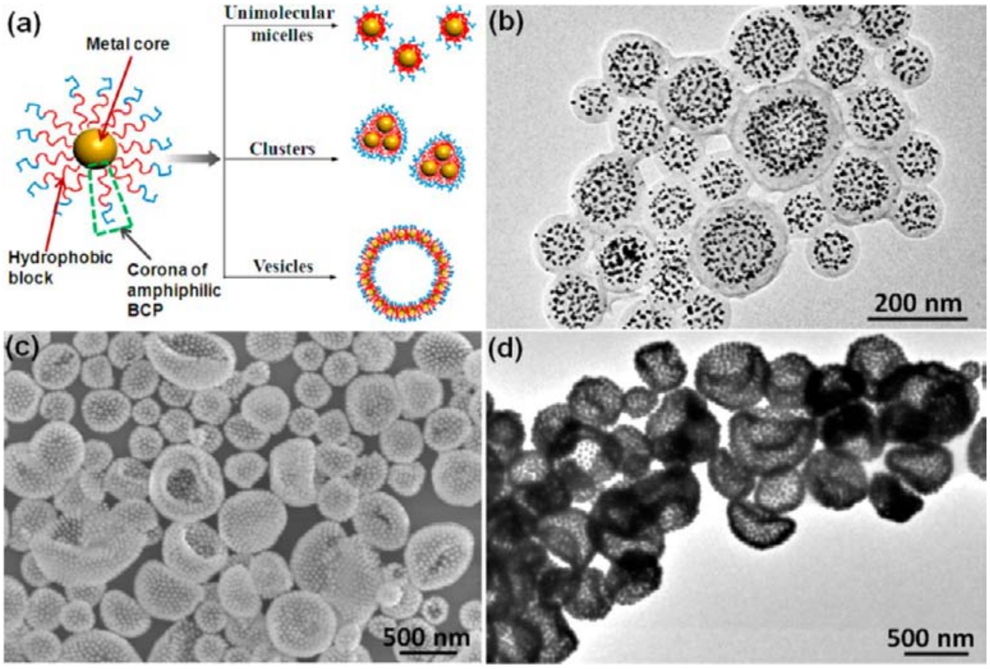

Figure 1. (a) Schematic illustration of APMNs composed of metal cores and amphiphilic BCP coronas, and the assembly structures. (b) Representative TEM image of vesicular assemblies of PS-34-Au-5. (c) SEM and (d) TEM images of vesicular assemblies of PS-34-Au-40.

Here, $\vec{r}_{ij} = \vec{r}_i - \vec{r}_j$, $r_{ij} = |\vec{r}_{ij}|$,$\vec{e}_{ij} = \vec{r}_{ij}/r_{ij}$, r_c is the interaction cutoff radius, and $\vec{v}_{ij} = \vec{v}_i - \vec{v}_j$. θ_{ij} is a random number with Gaussian distribution and unit variance. α_{ij} is the interaction parameter between beads i and j. The weight functions $w^D(r_{ij})$ and $w^R(r_{ij})$ of dissipative and random forces couple together to form a thermostat. Español and Warren showed the correct relation between the two functions:[41]

$$w^D(r_{ij}) = [w^R(r_{ij})]^2$$

$$\sigma^2 = 2\gamma k_B T \tag{3}$$

In this work, we adopted 8 linear chains connected to a center NP core to form the composite system $C_{90}(A_xB_y)_8$, where the hydrophobic PS is denoted as type A and hydrophilic PEO is denoted as type B, and C_{90} represents the AuNPs, in which 90 CG beads form a spherical rigid body.[42] Each composite system contains $N_b = 8(x + y) + 90$ beads, in which x is the length of an A block, and y is the length of a B block.

Coarse-Grain Mapping. To map onto these experimental systems of AuNPs tethered with BCPs, we chose an appropriate coarse-graining level for water, PEO, PS and AuNPs. Take 40 nm AuNP as an example, the diameter of the rigid body C90 was set as 4.0 in reduced units in our simulations. The corresponding CG models of water, PEO and PS were then determined by this coarse-graining level (see SI for details). Since PEO is miscible with water at almost any concentrations, and AuNP and PS dislike water, DPD interaction parameters $\alpha_{BS} = 27$ and $\alpha_{CS} = \alpha_{AS} = 80$ were used here. We fixed interaction parameter between the same type of beads at $\alpha_{ii} = 25$ to describe the compressibility of water, and set $\alpha_{AB} = 40$ to make sure that the microphase separation between A and B components will occur.

2.5. Cytotoxicity Test. The cytotoxicity of assembled nanostructures was evaluated using standard 3-(4,5-dimethylthiazol-2-yl)-2,5-diphenyltetrazolium bromide (MTT) assay protocol. Briefly, 4T1 breast cancer cells were incubated with various concentrations of assemblies (6.25−100 μg/mL) for 24 h. The medium was replaced with 200 μL of fresh medium including 20 μL of MTT solution (5 mg/mL), and the wells were further incubated for 4 h. The medium was then removed, and 150 μL of dimethyl sulfoxide (DMSO) was added into each well to dissolve the internalized purple formazan crystals. An aliquot of 100 μL was taken from each well and transferred into a fresh 96-well plate. The absorption at 570 nm was measured using a microplate reader. The absorption from the control cells was set as 100% cell viability.

2.6. Bioimaging of 4T1 Cells Using Multiphoton Absorption Induced Luminescence (MAIL). 4T1 breast cancer cells were plated for 24 h prior to the experiment in chamber slides at a cell density of 5 × 10^3 cell/cm^2. After incubation with 0.05 mg/mL particles for 3 h, the 4T1 cells were then washed twice with PBS and were fixed with Z-fix solution (Anatech) for 20 min. The slides were washed twice with PBS and then examined with a multiphoton excitation confocal microscope (Zeiss LSM). The laser was tuned to 800 nm for excitation, and the laser power was about 2 mW. The MAIL emission signal was collected in a wide spectrum of 470−600 nm with a spectral resolution of 20 nm.

2.7. Photothermal Treatment with NIR Light. To study the dynamic photothermal effect, the APMN assemblies were dispersed in distilled water. Briefly, 0.5 mg/mL of APMN solutions were irradiated with an 808 nm NIR laser (LaserGlow Technologies, 1 W cm^{-2}). Real-time thermal imaging of solution was recorded using a thermal camera (FLIR). The quantification analysis was performed by FLIR Examiner software. 4T1 breast cancer cells were plated for 24 h before the start of the experiment in 96 wells at a density of 1 × 10^4 cell/well. The cells were incubated with 0.05 mg/mL particles at 37 °C. After the internalization of APMNs for 3 h, an 808 nm NIR laser was used to irradiate cells at a power density of 1 W cm^{-2} for 5 min. A standard cell viability assay using MTT was conducted to determine the cell killing efficiency after photothermal ablation.

For *in vivo* studies, mice bearing 4T1 tumors were intratumorally injected with 50 μL of 2 mg/mL assemblies and then were irradiated with the 808 nm NIR laser at power density of 1 W cm^{-2} for 5 min. Mice treated with the same volume of saline and irradiated with laser without particles were used as a control. Real-time thermal imaging of 4T1 tumors was monitored with FLIR. After treatment, the 4T1 tumor volume was monitored. Tumor dimensions were determined at various time points using a caliper. Tumor volume (V) (mm^3) was calculated using the following formula: $V = a \times b^2/2$, where a is the length and b is the width in millimeters, respectively. Relative tumor volumes were calculated as V/V_0, where V_0 is the original tumor volume before the treatment was initiated.

2.8. Characterizations. The M_ws and M_w distribution of BCPs were measured by gel permeation chromatography (GPC) using a Viscotek system equipped with a refractive index detector (RI 410) and four columns at 45 °C. THF was used as the eluent at an elution rate of 1 mL min^{-1}, and polystyrene standards were used for calibration. ^{1}H NMR spectra were recorded with a Bruker AV-400 MHz high-resolution NMR spectrometer in $CDCl_3$. The UV−vis spectra of AuNPs and assemblies were taken on a PERKIN LAMBDA 35 UV−vis system. The morphologies of assemblies were imaged using a Hitachi SU-70 Schottky field emission gun scanning electron microscope (FEG-SEM) and a JEOL FEG transmission electron microscope (FEG-TEM). Samples for SEM were prepared by casting a 5−10 μL of aqueous solution of NPs on silicon wafers and dried at room temperature. TEM samples were prepared by casting 3−5 μL of NP solution onto 300 mesh copper grids covered with carbon film and dried at room temperature. To obtain the 3D structure of vesicles, TEM images were recorded while tilting the specimen through an angle range of −72 to 60° with a 3° increment, using Tecnai TF30 electron microscope operating at an accelerating voltage of 300 kV. The IMOD software was used to generate the tomogram or slices through the volume, which were segmented and surface rendered using Amira software. The hydrodynamic diameter of assemblies in solution was measured using a Nano Particle SZ-100 (HORIBA Scientific) light scattering instrument at a scattering angle 90°.

3. RESULTS AND DISCUSSION

3.1. Self-Assembly Behavior of APMNs in Mixed Solvents. The synthesis of the APMNs was achieved by covalently tethering PEO-*b*-PS-SH on the surface of AuNPs through Au−S bonds (Figure 1a). The obtained APMNs were denoted as PS-X-Au-D hereafter, where X and D indicate the M_w of PS blocks ($X = M_w/1000$) and the diameter of AuNPs, respectively. The average grafting density of BCPs was estimated to be ~0.1 chain per nm^{-2}, depending on the BCP M_w and surface curvature of AuNPs.[15] The predesigned BCP tethers ensured the well-defined chemical structures and polymer lengths of APMNs.

The self-assembly of APMNs was triggered by adding water into a THF solution of APMNs (0.5 mg/mL), followed by the dialysis of the solution against water to remove the organic solvent. The addition of water, which is a poor solvent for PS, collapses PS blocks to minimize the overall free energy of the system, resulting in the assembly of APMNs into unimolecular micelles, clusters, and vesicles. The representative SEM and TEM images in Figure 1b−d show the vesicular assemblies of PS-34-Au-5 and PS-34-Au-40 (see more images in SI). The vesicles are composed of a single layer of densely packed AuNPs separated by polymers between AuNPs in the vesicular membranes. The hollow interiors of the vesicles are clearly indicated by the buckling of vesicles in SEM and TEM images (Figure 1c,d). For PS-49-Au-20, the image recorded and reconstructed as a 3-D electron density mapping further confirms the inner cavity of vesicles (Figure S1 and movie). The dimensions of vesicles can be tuned by varying the size of Au cores. Rather monodispersed vesicles with an average size of 117.1 ± 18.2 nm were obtained for PS-34-Au-5, while the size of vesicular assemblies of PS-34-Au-40 increased up to 480.9 ± 121.1 nm.

The assembly of AuNPs reduces the distance between particles, resulting in a red-shift in the LSPR peak, due to the plasmonic coupling of adjacent AuNPs. This process is accompanied with a color change of the solution from dark-red to purple. By varying the content of water, the critical water concentration (C_{CWC}) can be determined by monitoring the shift in the extinction spectra (Figure 2a). Upon the slow addition of water until 20 vol % (1 vol % every 3 min), the plasmonic peak of PS-49-Au-20 gradually red-shifted from 528 to 551 nm. Figure 2b plots the variation in the plasmonic peaks of AuNPs as a function of water concentration. The C_{CWC} was defined as the onset of abrupt increase of plasmonic peaks. For 20 nm AuNPs, the C_{CWC} decreased from 12.1 to 9.5 vol % with the increase of M_w of PS blocks from 26 to 49 k. Noteworthy, the C_{CWC} of APMNs is slightly higher than that of linear amphiphilic BCPs of PEO-*b*-PS.[43,44] A higher water concentration required for APMN assembly implies that individual APMNs contribute less toward the overall free energy than individual polymers in conventional assembly of linear BCPs. This energy contribution is even less for individual polymer chains on NPs considering the multiple chains on each NP. We noticed that the concentration of water did not have an obvious impact on morphological transition of assemblies.

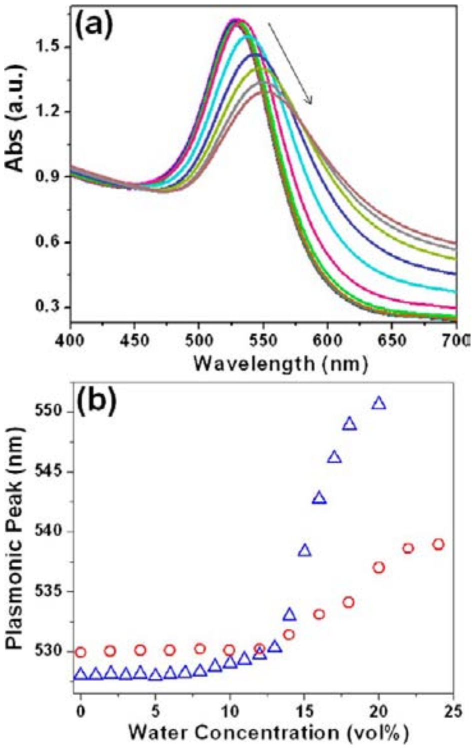

Figure 2. Determination of the C_{CWC} in the assembly of APMNs using UV−vis spectroscopy. (a) The UV−vis spectra of PS-49-Au-20 in the course of water addition (1 vol % per 3 min). (b) Plotting the plasmonic peak of PS-49-Au-20 (Δ) and PS-26-Au-20 (○) as a function of water concentration. The C_{CWC} was defined as the onset of abrupt increase in plasmonic peaks.

We evaluated the effect of polymer length on the assembly morphologies using 20 nm AuNPs as a model system. With the increase of M_w of PS blocks of BCP tethers from 7 k to 49 k, the assembly morphologies transited from unimolecular micelles (Figure 3a,d) to clusters (Figure 3b,e) and eventually to vesicles (Figure 3c,f) in selective solvents of water/THF (see Figure S1−3 for the low-magnification images). The corresponding average aggregation number (N_{agg}) of the APMNs in assemblies increased from ~1 to 2.2 and to 29. For a short PS block of 7 and 14 k, the unimolecular micelles ($N_{agg} \approx 1$) composed of discrete APMNs molecule were favorable. The increase of hydrophobic blocks led to a rapid increase in N_{agg} to 2.2 for a mixture of dimers (55%) and trimers (27%) assembled from PS-24-Au-20 and to 29 for vesicles of PS-49-Au-20 system.

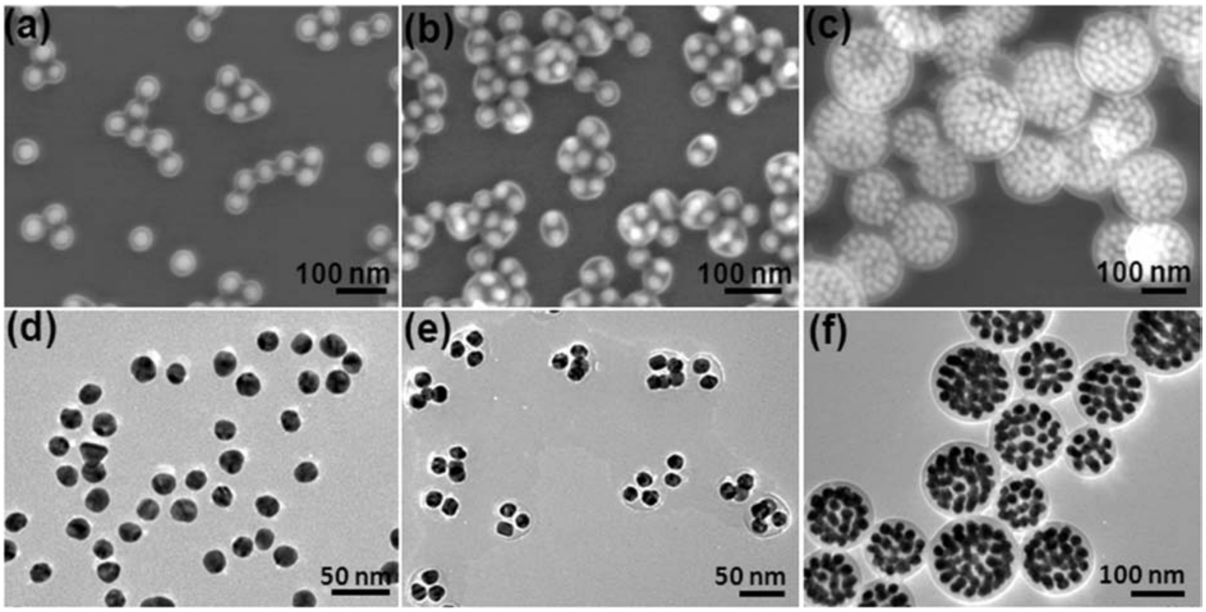

Figure 3. (a−c) SEM and (d−f) TEM images of Au-20 assemblies using various M_w of BCPs: (a,d) PS-14; (b,e) PS-24; and (c,f) PS-49.

Qualitatively, the average N_{agg} was exponentially correlated to the M_w of PS blocks as $N_{agg} \sim N_{PS}^{3.2}$, where N_{PS} is the number of repeating units of styrene in BCP chains (Figure 4a). The N_{agg} of APMNs shows a much stronger dependence on the M_w of PS than that of linear BCP system which follows $N_{agg} \sim N_{PS}^{0.8-1.2}$.[45] This can be attributed to the multiple polymer chains in each APMN. This study establishes a facile approach to control N_{agg} in AuNP clusters by simply tuning M_w of PS. Our method shows advantages, such as simplicity, scalability, and low cost, over existing approaches, including DNA-driven assembly and top-down method for the fabrication of AuNP clusters,[46−50] although it sacrifices precision and monodispersity to certain extent. The increase in N_{agg} with increasing PS M_w was also confirmed by the variation in the hydrodynamic diameters (D_H) of assemblies using dynamic light scattering (DLS) (Figure 4b). The D_H of unimolecular micelles of PS-8-Au-20 and PS-14-Au-20 are ~49 and 52 nm, respectively; these values are in a good agreement with the overall diameter of AuNPs with a polymer shell. The D_H of vesicular micelles of PS-49-Au-20 is ~151 nm, which is consistent with the results obtained from TEM and SEM measurements (182.8 ± 13.6 nm). Overall, the assemblies with different morphologies showed a relatively uniform size distribution in solution, as indicated by the narrow distribution of hydrodynamic diameter in DLS.

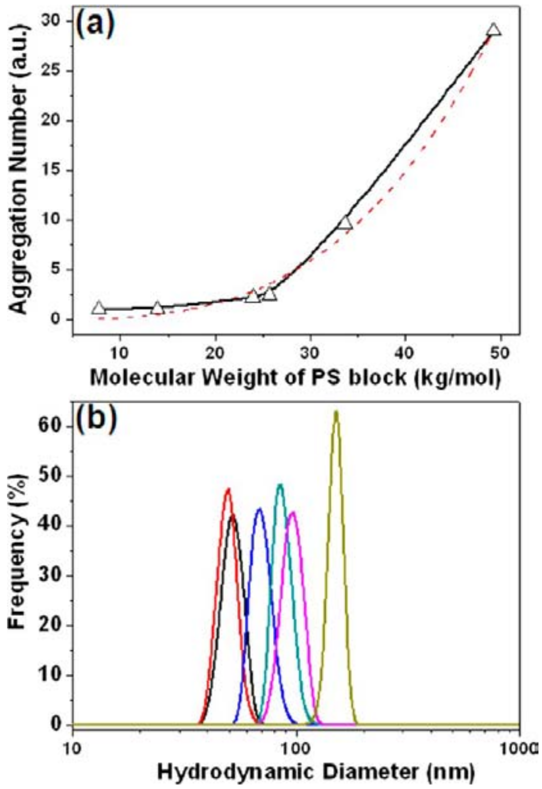

Figure 4. (a) The increase of average aggregation number with the M_w of PS block. The dash line is the theoretical aggregation number, fitted using the power law, $y = a_0x^{3.2}$. (b) The hydrodynamic diameters of Au-20 assemblies using different M_w of BCPs. The M_w of PS increase from 7.7 to 49 k from left to right.

3.2. Simulation and Modeling the Self-Assembly Behavior. It is known that the self-assembled structures of molecular amphiphiles can be quantitatively determined by the geometrical packing parameter, $P = \nu/a_o l_c$, where a_o is the area of hydrophilic portions, and ν and l_c are the volume and length of hydrophobic compartments, respectively.[51−53] With the increase of P, the assembly of molecular amphiphiles undergoes morphological transition from spherical, to cylindrical micelles, and to vesicles/planar bilayers eventually.[52] However, the conventional packing theory cannot interpret the formation of different morphologies in the self-assembly of APMNs.[54] The assembly morphologies are determined not only by the relative fraction of hydrophilic and hydrophobic blocks but also by the size of Au cores (Figure 5). In contrast to linear BCPs, the variation in the dimension of metal cores led to the transition of final morphologies of APMN assemblies at a given M_w of BCPs. For example, the assembly morphologies of APMN carrying PS-24k transited from unimolecular micelles, to clusters, and eventually to vesicles, with the decrease of the sizes of Au cores. This can be ascribed to the fact that the restriction of metal

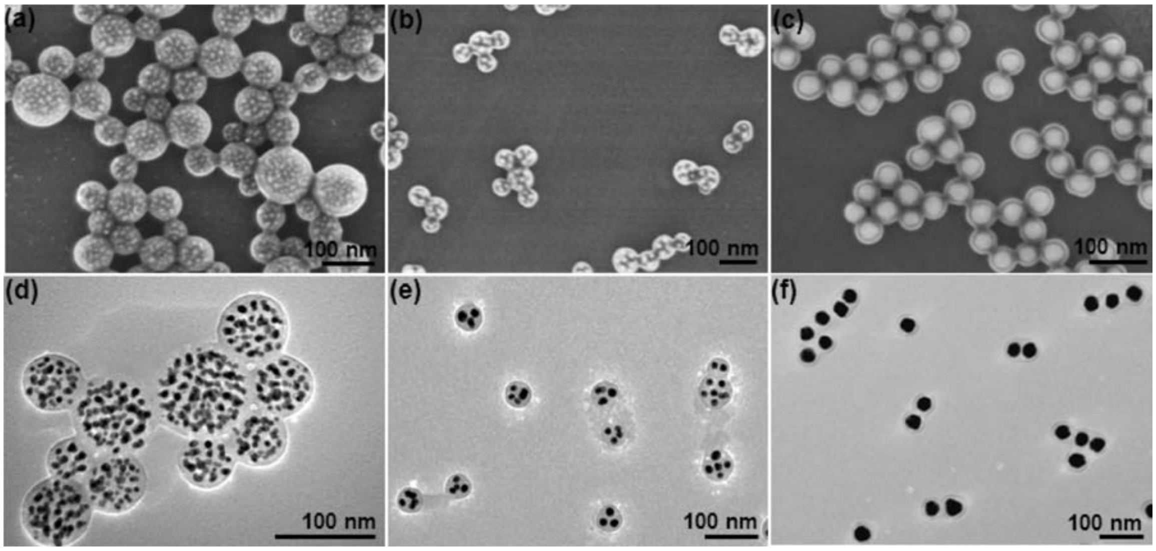

Figure 5. (a−c) SEM and (d−f) TEM images of APMNs PS-24 assemblies using various sizes of Au cores: (a,d) Au-5; (b,e) Au-15; and (c,f) Au-30.

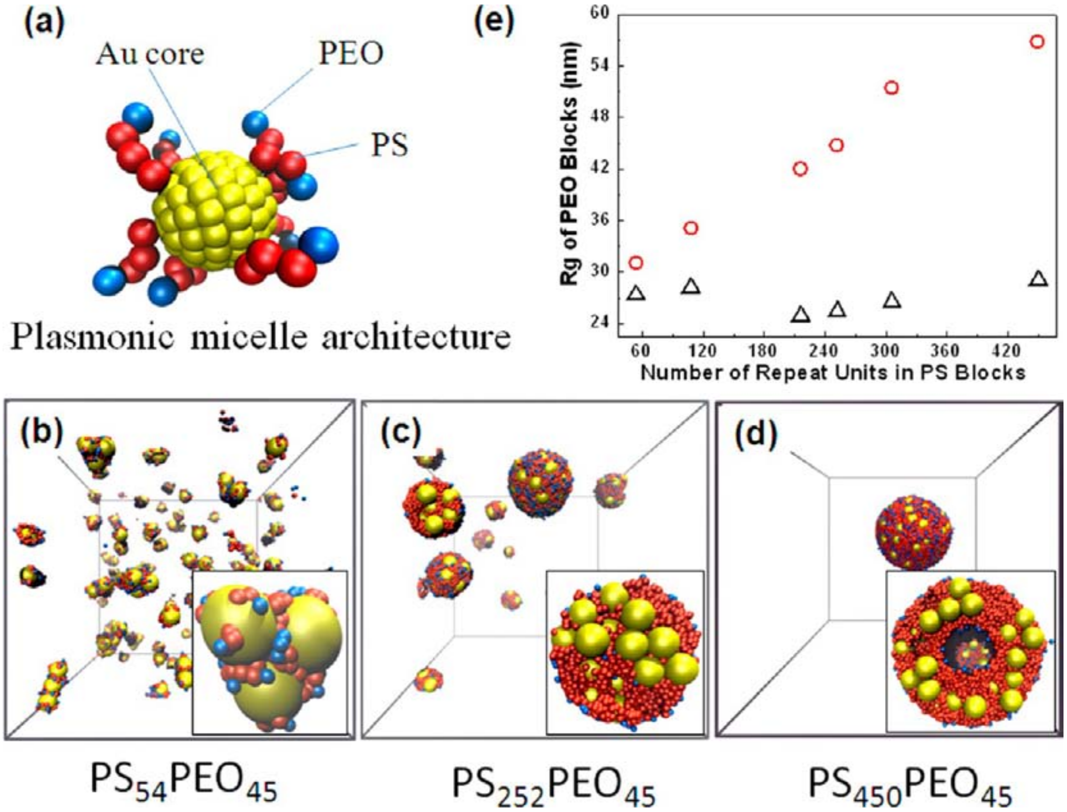

Figure 6. DPD simulation of the self-assembly of APMNs using a CG model. (a) A representative architecture of AuNP tethered with 8 short linear block copolymer chains $C_{90}(A_3B_1)_8$. There are 4 CG beads in each chain, with 3 red beads and 1 blue bead representing A and B blocks, respectively, where A denotes PS component and B denotes PEO component. 90 yellow beads represent the center AuNP, which is taken as a rigid body in our simulations. (b−d) The assembled structures obtained in DPD simulations: (b) unimolecular micells and small clusters, (c) large clusters, and (d) vesicles. (e) The R_g of all the CG beads of PEO blocks on an individual AuNP as a function of the chain length of PS block before (Δ) and after (○) assembly.

cores has a significant influence on the conformation of BCP chains, e.g., the stretching and compacting of polymers.

In terms of the overall free energy associated with the segregation of individual polymer chains during the micellization of amphiphiles, the entropic and enthalpy contributions of individual BCPs immobilized on AuNPs are much less than those of free linear BCPs in conventional assembly systems. First, the PEO hydration outer layers of the core−shell-like APMNs causes a strong "steric effect" during the intermolecular collapse of PS blocks on neighboring particles. This would sacrifice the enthalpic contribution of individual polymer chains of AMNPs to the over free energy. Second, the confinement of PS blocks beneath the "shielding" PEO layers limits the interactions of hydrophobic PS blocks with water molecules.

This significantly decreases the entropy gain originated from excluding water molecules surrounding hydrophobic blocks.[55] In a word, the delicate interplay of enthalpy/entropy contribution to the overall free energy, strongly depending on the spherical architecture of APMNs, yields the diagram of different assemblies.

For a better understanding of the self-assembly mechanism of APMNs, we performed DPD simulation of the self-assembly of APMNs using a CG model. To map these experimental systems of APMNs, we chose an appropriate coarse-graining level for solvent, PEO, PS, and AuNPs (see Tables S1 and S2). Our DPD simulation is in good agreement with experimental observations: The APMN assemblies underwent transition from unimolecular micelles, to clusters, and to vesicles with increasing length of PS block (Figure 6). To establish the correlation between the geometric and chemical parameters of APMNs and the resulting morphologies of assemblies, we calculated the radius of gyration (R_g) of all the CG beads of PEO blocks on an individual AuNP. For an individual AuNP tethered with BCP chains in aqueous solution, all the PS chains are prone to be adsorbed on NP surface and aggregate to form a "PS droplet", and the end PEO blocks are distributed separately on the surface of the "PS droplet". We found that before the occurrence of assembly, the R_g of PEO beads for APMNs with PS of different chain lengths is almost independent of the length of PS block, due to the aggregation of PS blocks (Figure 6e). However, for APMNs in self-assembled entities, the R_g of PEO beads approximately linearly increases with the increase in the length of PS block. This is accompanied with the morphological transition of self-assembly. For example, for A17B1 and A25B1 in self-assembled structures, the R_g of PEO beads is 51 and 56 nm, which are much larger than their corresponding values in the case of individual NP (about 26 and 29 nm), respectively. This indicates that the deformability of the effective NPs (that is, NP together with tethered chains as a whole) is crucial to form the self-assembled structures. For NPs tethered with short chains, the PS chains are not long enough to allow redistribution of PEO beads on the NP surface, so the NPs can only aggregate to form small clusters. For long enough PS chains, the tethered NPs are effectively deformable. When several NPs approach each other, the PS chains can accommodate new configurations and allow redistribution of PEO beads on the NP surface. When PEO beads can be redistributed on both sides of the NP during aggregation, the larger R_g of PEO beads enables the assembly of APMNs into vesicular structures.

The sizes of "micelle" core and the lengths of amphiphilic corona BCPs of APMNs can be independently and precisely tuned, which is not readily attainable by first-level molecular self-assembly approaches. This allows us to systematically study the effect of length of BCP tethers and the size of AuNP cores on the assembled nanostructures. The corresponding results are summarized in a phase diagram (Figure 7). Overall, the unimolecular micelles were mainly formed with low M_w of polymer tethers and large sizes of AuNPs. The increase of polymer M_w and decrease of sizes of Au cores led to the formation of vesicles. At medium lengths of polymer tethers and sizes of Au cores, clusters were obtained.

3.3. Plasmon Couplings of Assemblies. The control over the NP size (D), N_{agg}, and interparticle distance (d) in the assembly of APMNs allows the fine control over the near-field plasmon coupling of AuNPs. For near-field plasmon coupling of AuNPs, the shift in the LSPR peaks of AuNP pairs is proportional to $e^{-(d/D)}$ and the decay constant of plasmon coupling is ~0.23.[56,57] When M_w of PS blocks increased, the extinction spectra of assemblies obtained from Au-20 displayed a large red-shift with the increase of N_{agg} (Figure 8b), despite a slight increase of interparticle distance.

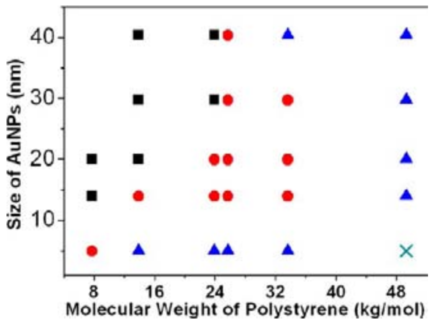

Figure 7. Phase diagram of the self-assembly of APMNs with different M_w of BCPs and sizes of AuNPs: unimolecular micelles (■); clusters (●); vesicles (▲); and precipitates (×).

In the weak coupling range ($0.23 \leq d/D \leq 0.5$), the red-shift in plasmonic peak with the increase of BCP M_w is due to the increase in the number of the interstitial junctions of AuNPs, along with the morphological transition from unimolecular micelles to vesicles.[58−60] This was also confirmed by the plasmonic properties of Au-5 (see Figure S6), Au-14 (Figure 8a), and Au-30. Note that, in this range, the increase of AuNP sizes (e.g., from Au-14 to Au-20) only induced a small red-shift in plasmon peak, as a result of weak coupling. However, in the strong coupling range ($d/D \leq 0.23$), the assemblies of Au-40 (see Figure S8) displayed not only a significantly larger magnitude of plasmon shift but also the splitting of plasmon peak into two well-defined plasmonic peaks (Figure 8c,d). The vesicular assemblies of PS-34-Au-40 and PS-49-Au-40 showed plasmonic peaks located at 577 and 709 nm and 581 and 743 nm, respectively. We presume that it is due to the occurrence of "plasmon hybridization", analogous to hollow Au nanoshells.[61] The two plasmon peaks correspond to the symmetric and asymmetric plasmon coupling models of vesicle shell, which only occurs under a strong plasmon coupling between AuNPs. It is not surprising that the hybridization was only observed in the vesicles of Au-40 in which a strong plasmon coupling occurred at a given interparticle distance (i.e., constant polymer shell thickness in between AuNPs). To the best of our knowledge, this is the first observation of plasmon hybridization in vesicular assemblies of discrete NPs.

The emerging collective optical properties of assembled APMNs are of interest for biomedical applications, e.g., bioimaging and photothermal therapy for cancer treatment. As a result of field-enhanced multiphoton absorption, AuNP aggregates are known for their intense MAIL that is strongly correlated to N_{agg} of assemblies.[62,63] For a demonstration, 4T1 cancer cells were chosen and incubated with various assemblies of Au-20 for 3 h at a concentration of 0.05 mg/mL. MAIL imaging of the cells was obtained by excitation with 800 nm light and recording in a wide spectra of 470−600 nm after the removal of free particles (Figure 9a). The luminescence images of 4T1 cells clearly showed the well distribution of various assemblies in the cytoplasm. The high contrast of red luminescence suggests an efficient cell uptake of the assemblies. The MAIL signal gradually increased with the increase of N_{agg} of assemblies due to a stronger coupling of electromagnetic

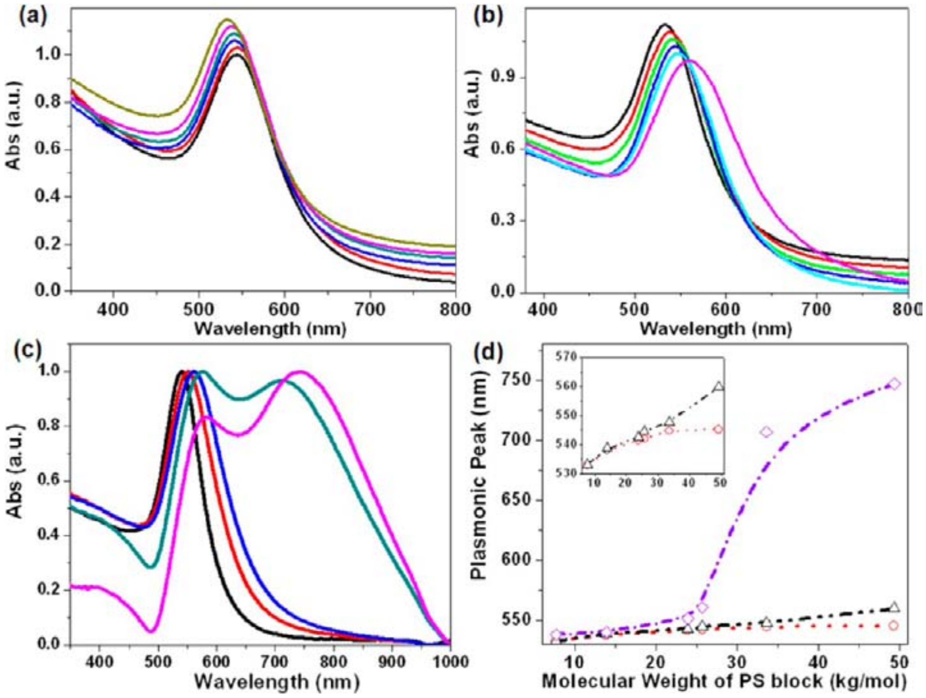

Figure 8. (a−c) UV−vis spectra of (a) Au-14, (b) Au-20, and (c) Au-40 using different M_w of BCPs. The M_w of BCPs monotonically increased from left to right, along with the red-shift of plasmonic peaks. (d) Plasmonic peaks of Au-14 (○, red), Au-20 (Δ, black) and Au-40 (◇, purple) assemblies showing in (a−c) plotted as a function of M_w of PS block. The inset in (d) shows the plasmonic peaks of Au-14 (○, red) and Au-20 (Δ, black).

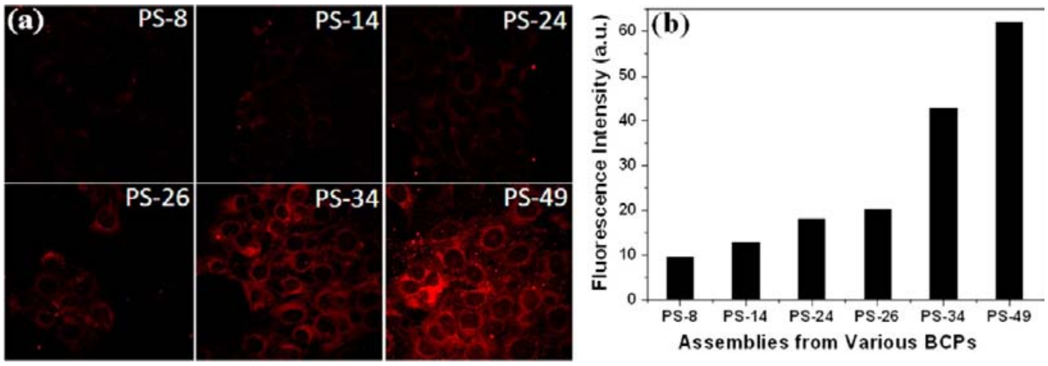

Figure 9. (a) MAIL images of 4T1 cancer cells loaded with assemblies from various BCPs for 3 h at a concentration of 0.05 mg/mL. (b) The average fluorescence intensity of MAIL images shown in (a).

field for larger ordered assemblies (Figure 9b). The advantage of MAIL images is the excitation light at the wavelength of 800 nm which is penetrable deeply into human tissues; and no degradation or hazard metal ions would be released for our AuNP assemblies, unlike traditional organic dyes or quantum dots.[64,65]

3.4. Photothermal Therapy. The plasmon hybridization for Au-40 vesicles resulted in a strong absorption in the NIR range, thus facilitating their applications in photothermal therapy. To demonstrate the concept, we first evaluated the photothermal effect of Au-40 assemblies in distilled water. The rising of solution temperature was mapped and quantified by real-time thermal imaging using a thermal camera (FLIR). As shown in Figure 10, the temperature of solution gradually increased with the prolonged irradiation time of laser. Figure 10a shows the temperature distribution of solution exposed to NIR laser at 808 nm. The pathway of laser beam in solution readily changed the color from blue to red, indicating the rising of solution temperature. No obvious temperature change was observed in control experiments of pure water. For unimolecular micelles, no obvious laser pathway was observed in solution due to the smaller increase in temperature. In the case of PS-14-Au-40 vesicles, the NIR irradiation induced the increase in the solution temperature >40 °C within 68 s and >60 °C within 300 s (Figure 10b). Such photothermal effect is much stronger than that of discrete AuNPs as reported previously, especially considering the current use of an excitation light at 808 nm.[66−70]

The vesicular assemblies were further chosen for subsequent biological study. The efficient heating upon irradiation enables the application of such structures for photothermal therapy.[71,72] To investigate the photothermal therapy effect, 4T1 cancer cells incubated with vesicles of PS-14-Au-40 (0.05 mg/mL) were exposed to NIR laser of 808 nm (1 W cm^{-2}) for 5 min. After irradiation, the photothermal ablation of breast cancer cells was explored using a standard MTT assay. Compared to the control group without using vesicles, the cell viability was only 7.2 ± 3.4% in the treated group (see Figure S11).

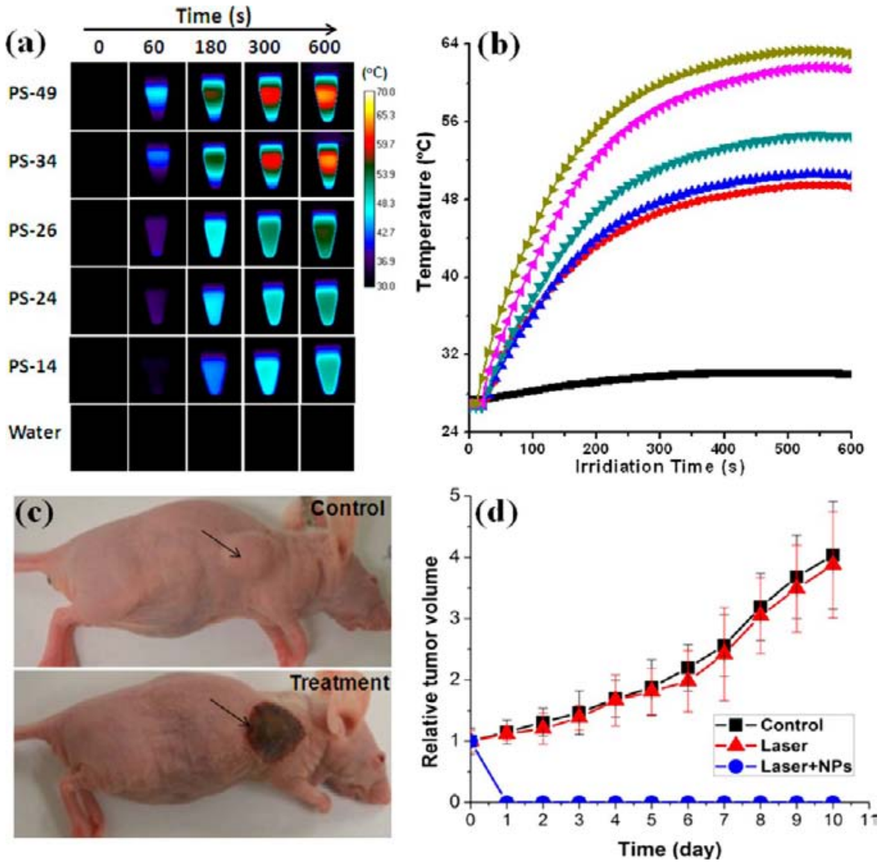

Figure 10. (a) Temperature mapping during the 808 nm laser irradiation (1 W cm^{-2}) of Au-40 assemblies in distilled water by real-time thermal imaging using a thermal camera (FLIR). (b) Temperature profiles were plotted as a function of irradiation time, using the different assemblies of Au-40: decrease of polymer M_w from top to bottom. The black curve is recorded from pure water. (c) Mice were treated with and without PS-14-Au-40 vesicles under laser irradiation. (d) The tumor growth curves of different groups of mice after treatment.

The *in vivo* studies were performed using a 4T1 tumor xenograft model. Nude mice bearing 4T1 tumors were intratumorally injected with PS-14-Au-40 vesicles (2 mg/mL) and then subjected to the 808 nm laser exposure. The local temperature change in mice was monitored with a FLIR. The temperature of tumor injected with vesicles under NIR laser irradiation rapidly increased to 55−60 °C within 1 min which is high enough to kill tumor *in vivo* (see Figure S11). The *in vivo* therapeutic efficacy of PS-14-Au-40 vesicles was also evaluated. Figure 10c presented that the tumors treated with particles under laser irradiation were effectively ablated, leaving black scars at the tumor sites without showing reoccurrence. In contrast, the tumors in control groups showed similar growth speed (Figure 10d). Noteworthy that, the vesicular assemblies are particularly interesting for the *in vivo* photothermal therapy by taking account of the easy clearance of them after dissociation.

4. CONCLUSIONS

In summary, we have systematically studied the hierarchical self-assembly of APMNs composed of Au cores and amphiphilic BCP tethers in selective solvents. The assembly of APMNs resembles the secondary self-assembly of polymeric micellar architectures. Depending on the relative sizes of Au cores and lengths of polymer tethers, APMNs assembled into unimolecular micelles, clusters, and vesicles in the mixed solvent of water/THF. Computer simulation results suggest that the mobility of PEO segments on APMNs plays a critical role in the assembly of APMNs into larger assemblies. Longer PS blocks would give rise to a higher mobility of PEO segments on APMNs, thus leading to the assembly of vesicular structures, while shorter PS blocks led to the formation of unimolecular micelles. In addition, the fine control over the assembly of such APMNs enabled us to modulate the plasmon coupling between discrete AuNPs in the assemblies, thus their superior performance of the assemblies in MAIL-based cell imaging, and photothermal therapy for cancer treatment. Further use of NPs with various geometries and shapes as the cores of APMNs will create micelle-like architectures, beyond the capability of conventional approaches, for assembling complex structured materials. This study will not only offer new insights into the understanding of hierarchical self-assembly of polymer micelles but also contribute to the development of new concepts of plasmon polymers.[28]

■ ASSOCIATED CONTENT

Ⓢ Supporting Information

The details of DPD simulation, more SEM/TEM images of various assemblies and cell viability at various concentrations of assemblies. This material is available free of charge via the Internet at http://pubs.acs.org.

■ AUTHOR INFORMATION

Corresponding Author

luzhy@jlu.edu.cn; shawn.chen@nih.gov; znie@umd.edu

Author Contributions

$^{\#}$These authors contributed equally.

Notes

The authors declare no competing financial interest.

■ ACKNOWLEDGMENTS

Z.N. acknowledges financial support of startup funds from the University of Maryland. X.C. thanks the Intramural Research Program (IRP) of the NIBIB, NIH. T.B. thanks the support of the Arnold and Mabel Beckman Foundation. We also acknowledge the support of the Maryland NanoCenter and its NispLab and FabLab. The NispLab is supported in part by the NSF as a MRSEC Shared Experimental Facilities.

■ REFERENCES

(1) Groschel, A. H.; Schacher, F. H.; Schmalz, H.; Borisov, O. V.; Zhulina, E. B.; Walther, A.; Muller, A. H. E. *Nat. Commun.* **2012**, *3*, 710.

(2) Rupar, P. A.; Chabanne, L.; Winnik, M. A.; Manners, I. *Science* **2012**, *337*, 559.

(3) Wang, Z. P.; van Oers, M. C. M.; Rutjes, F. P. J. T.; van Hest, J. C. M. *Angew. Chem., Int. Ed.* **2012**, *51*, 10746.

(4) Thompson, K. L.; Chambon, P.; Verber, R.; Armes, S. P. *J. Am. Chem. Soc.* **2012**, *134*, 12450.

(5) Jin, H. B.; Huang, W.; Zhu, X. Y.; Zhou, Y. F.; Yan, D. Y. *Chem. Soc. Rev.* **2012**, *41*, 5986.

(6) Fang, B.; Walther, A.; Wolf, A.; Xu, Y. Y.; Yuan, J. Y.; Muller, A. H. E. *Angew. Chem., Int. Ed.* **2009**, *48*, 2877.

(7) Walther, A.; Muller, A. H. E. *Soft Matter* **2008**, *4*, 663.

(8) Mai, Y. Y.; Eisenberg, A. *Chem. Soc. Rev.* **2012**, *41*, 5969.

(9) Hu, J.; Zhang, G.; Liu, S. *Chem. Soc. Rev.* **2012**, *41*, 5933.

(10) Yan, D. Y.; Zhou, Y. F.; Hou, J. *Science* **2004**, *303*, 65.

(11) Pochan, D. J.; Chen, Z. Y.; Cui, H. G.; Hales, K.; Qi, K.; Wooley, K. L. *Science* **2004**, *306*, 94.

(12) Gao, Y.; Wang, Y. F.; Jiang, M.; Chen, D. Y. *ACS Macro Lett.* **2012**, *1*, 1312.

(13) Grzelczak, M.; Sanchez-Iglesias, A.; Mezerji, H. H.; Bals, S.; Perez-Juste, J.; Liz-Marzan, L. M. *Nano Lett.* **2012**, *12*, 4380.

(14) Hu, J. M.; Wu, T.; Zhang, G. Y.; Liu, S. Y. *J. Am. Chem. Soc.* **2012**, *134*, 7624.

(15) He, J.; Liu, Y.; Babu, T.; Wei, Z.; Nie, Z. *J. Am. Chem. Soc.* **2012**, *134*, 11342.

(16) Song, J. B.; Cheng, L.; Liu, A. P.; Yin, J.; Kuang, M.; Duan, H. W. *J. Am. Chem. Soc.* **2011**, *133*, 10760.

(17) Guo, Y.; Harirchian-Saei, S.; Izumi, C. M. S.; Moffitt, M. G. *ACS Nano* **2011**, *5*, 3309.

(18) Mai, Y.; Eisenberg, A. *J. Am. Chem. Soc.* **2010**, *132*, 10078.

(19) Nie, Z. H.; Fava, D.; Kumacheva, E.; Zou, S.; Walker, G. C.; Rubinstein, M. *Nat. Mater.* **2007**, *6*, 609.

(20) Zubarev, E. R.; Xu, J.; Sayyad, A.; Gibson, J. D. *J. Am. Chem. Soc.* **2006**, *128*, 15098.

(21) He, J.; Zhang, P.; Babu, T.; Liu, Y.; Gong, J.; Nie, Z. *Chem Commun* **2013**, *49*, 576.

(22) Liu, K.; Nie, Z. H.; Zhao, N. N.; Li, W.; Rubinstein, M.; Kumacheva, E. *Science* **2010**, *329*, 197.

(23) Li, F.; Josephson, D. P.; Stein, A. *ngew. Chem., Int. Ed.* **2011**, *50*, 360.

(24) He, J.; Wei, Z.; Wang, L.; Tomova, Z.; Babu, T.; Wang, C.; Han, X.; Fourkas, J. T.; Nie, Z. *Angew. Chem., Int. Ed.* **2013**, *52*, 2463.

(25) Niikura, K.; Iyo, N.; Higuchi, T.; Nishio, T.; Jinnai, H.; Fujitani, N.; Ijiro, K. *J. Am. Chem. Soc.* **2012**, *134*, 7632.

(26) Yu, X. F.; Zhang, W. B.; Yue, K.; Li, X. P.; Liu, H.; Xin, Y.; Wang, C. L.; Wesdemiotis, C.; Cheng, S. Z. D. *J. Am. Chem. Soc.* **2012**, *134*, 7780.

(27) Yu, X. F.; Zhong, S.; Li, X. P.; Tu, Y. F.; Yang, S. G.; Van Horn, R. M.; Ni, C. Y.; Pochan, D. J.; Quirk, R. P.; Wesdemiotis, C.; Zhang, W. B.; Cheng, S. Z. D. *J. Am. Chem. Soc.* **2010**, *132*, 16741.

(28) Nie, Z. H.; Petukhova, A.; Kumacheva, E. *Nat. Nanotechnol.* **2010**, *5*, 15.

(29) Chen, H. J.; Ming, T. A.; Zhao, L.; Wang, F.; Sun, L. D.; Wang, J. F.; Yan, C. H. *Nano Today* **2010**, *5*, 494.

(30) Halas, N. J.; Lal, S.; Chang, W. S.; Link, S.; Nordlander, P. *Chem. Rev.* **2011**, *111*, 3913.

(31) Grzelczak, M.; Liz-Marzan, L. M. *Langmuir* **2013**, *29*, 4652.

(32) Zhang, K. K.; Jiang, M.; Chen, D. Y. *Prog. Polym. Sci.* **2012**, *37*, 445.

(33) Martin, M. N.; Basham, J. I.; Chando, P.; Eah, S. K. *Langmuir* **2010**, *26*, 7410.

(34) Frens, G. *Nat. Phys. Sci.* **1973**, *241*, 20.

(35) Jain, P. K.; Lee, K. S.; El-Sayed, I. H.; El-Sayed, M. A. *J. Phys. Chem. B* **2006**, *110*, 7238.

(36) Groot, R. D.; Madden, T. J. *J. Chem. Phys.* **1998**, *108*, 8713.

(37) Qian, H. J.; Lu, Z. Y.; Chen, L. J.; Li, Z. S.; Sun, C. C. *Macromolecules* **2005**, *38*, 1395.

(38) Pons-Siepermann, I. C.; Glotzer, S. C. *ACS Nano* **2012**, *6*, 3919.

(39) Pons-Siepermann, I. C.; Glotzer, S. C. *Soft Matter* **2012**, *8*, 6226.

(40) Groot, R. D.; Warren, P. B. *J. Chem. Phys.* **1997**, *107*, 4423.

(41) Espanol, P.; Warren, P. *Europhys. Lett.* **1995**, *30*, 191.

(42) Nguyen, T. D.; Phillips, C. L.; Anderson, J. A.; Glotzer, S. C. *Comput. Phys. Commun.* **2011**, *182*, 2307.

(43) Zhang, L. F.; Eisenberg, A. *Polym. Adv. Technol.* **1998**, *9*, 677.

(44) Yu, K.; Eisenberg, A. *Macromolecules* **1996**, *29*, 6359.

(45) Riess, G. *Prog. Polym. Sci.* **2003**, *28*, 1107.

(46) Chen, G.; Wang, Y.; Tan, L. H.; Yang, M. X.; Tan, L. S.; Chen, Y.; Chen, H. Y. *J. Am. Chem. Soc.* **2009**, *131*, 4218.

(47) Wang, Y.; Chen, G.; Yang, M. X.; Silber, G.; Xing, S. X.; Tan, L. H.; Wang, F.; Feng, Y. H.; Liu, X. G.; Li, S. Z.; Chen, H. Y. *Nat. Commun.* **2010**, *1*, 87.

(48) Xu, X. Y.; Rosi, N. L.; Wang, Y. H.; Huo, F. W.; Mirkin, C. A. *J. Am. Chem. Soc.* **2006**, *128*, 9286.

(49) Claridge, S. A.; Liang, H. Y. W.; Basu, S. R.; Frechet, J. M. J.; Alivisatos, A. P. *Nano Lett.* **2008**, *8*, 1202.

(50) Yan, W. J.; Xu, L. G.; Xu, C. L.; Ma, W.; Kuang, H.; Wang, L. B.; Kotov, N. A. *J. Am. Chem. Soc.* **2012**, *134*, 15114.

(51) Zhang, J. X.; Li, X. D.; Li, X. H. *Prog. Polym. Sci.* **2012**, *37*, 1130.

(52) Israelachvili, J. N. *Intermolecular and surface forces*; 2nd ed.; Academic Press: London, 1991.

(53) Motornov, M.; Roiter, Y.; Tokarev, I.; Minko, S. *Prog. Polym. Sci.* **2010**, *35*, 174.

(54) Ahn, S.; Jung, S. Y.; Lee, S. J. *J. Phys. Chem. C* **2011**, *115*, 22301.

(55) Shen, H. W.; Zhang, L. F.; Eisenberg, A. *J. Phys. Chem. B* **1997**, *101*, 4697.

(56) Jain, P. K.; Huang, W. Y.; El-Sayed, M. A. *Nano Lett.* **2007**, *7*, 2080.

(57) Reinhard, B. M.; Siu, M.; Agarwal, H.; Alivisatos, A. P.; Liphardt, J. *Nano Lett.* **2005**, *5*, 2246.

(58) Yan, B.; Thubagere, A.; Premasiri, W. R.; Ziegler, L. D.; Dal Negro, L.; Reinhard, B. M. *ACS Nano* **2009**, *3*, 1190.

(59) Wang, H. Y.; Rong, G. X.; Yan, B.; Yang, L. L.; Reinhard, B. M. *Nano Lett.* **2011**, *11*, 498.

(60) Sanchez-Iglesias, A.; Grzelczak, M.; Altantzis, T.; Goris, B.; Perez-Juste, J.; Bals, S.; Van Tendeloo, G.; Donaldson, S. H.; Chmelka, B. F.; Israelachvili, J. N.; Liz-Marzan, L. M. *ACS Nano* **2012**, *6*, 11059.

(61) Prodan, E.; Radloff, C.; Halas, N. J.; Nordlander, P. *Science* **2003**, *302*, 419.

(62) Farrer, R. A.; Butterfield, F. L.; Chen, V. W.; Fourkas, J. T. *Nano Lett.* **2005**, *5*, 1139.

(63) Nah, S.; Li, L. J.; Fourkas, J. T. *J. Phys. Chem. A* **2009**, *113*, 4416.

(64) Derfus, A. M.; Chan, W. C. W.; Bhatia, S. N. *Nano Lett.* **2004**, *4*, 11.

(65) Resch-Genger, U.; Grabolle, M.; Cavaliere-Jaricot, S.; Nitschke, R.; Nann, T. *Nat. Methods* **2008**, *5*, 763.

(66) Haba, Y.; Kojima, C.; Harada, A.; Ura, T.; Horinaka, H.; Kono, K. *Langmuir* **2007**, *23*, 5243.

(67) Umeda, Y.; Kojima, C.; Harada, A.; Horinaka, H.; Kono, K. *Bioconjugate Chem.* **2010**, *21*, 1559.

(68) Gorelikov, I.; Field, L. M.; Kumacheva, E. *J. Am. Chem. Soc.* **2004**, *126*, 15938.

(69) Wang, J.; Zhu, G. Z.; You, M. X.; Song, E. Q.; Shukoor, M. I.; Zhang, K. J.; Altman, M. B.; Chen, Y.; Zhu, Z.; Huang, C. Z.; Tan, W. H. *ACS Nano* **2012**, *6*, 5070.

(70) Budhlall, B. M.; Marquez, M.; Velev, O. D. *Langmuir* **2008**, *24*, 11959.

(71) Huang, X. H.; El-Sayed, I. H.; Qian, W.; El-Sayed, M. A. *J. Am. Chem. Soc.* **2006**, *128*, 2115.

(72) Jain, P. K.; Huang, X. H.; El-Sayed, I. H.; El-Sayed, M. A. *Acc. Chem. Res.* **2008**, *41*, 1578.